Computation of spectral arrays in hot plasmas using the Lanczos algorithm

Balazs F. Rozsnyai, Stewart D. Bloom, and David A. Resler
Department of Physics, Lawrence Livermore National Laboratory, P.O. Box 808, Livermore, California 94550
(Received 15 April 1991)

We apply the approach initiated by Lanczos to compute large spectral arrays in hot plasmas. The wave functions that form the basis for the Lanczos state vectors are derived from a self-consistent "average-atom" model. We present calculations for a bromine plasma at low and at metallic density.

PACS number(s): 52.25.Rv

I. INTRODUCTION

When medium- or high-Z elements are partially ionized either in astrophysical or in laboratory plasmas the number of spectral lines can be enormous, which presents a serious problem for the computation of the photoabsorption cross section. There have been several ways to address this problem, all of which involve the accounting of many-electron states, only to the degree of level occupancies, that is to say to configurations, and account for the large number of angular momentum states in a statistical way. We will adopt the nomenclatures of *detailed configuration accounting* (DCA) and *detailed term accounting* (DTA) for the cases when only electronic configurations, or electronic configurations together with the definite J states are accounted, respectively. In the present work we use the term DCA with the understanding that we do not include configuration mixing. Electronic transitions due to photoabsorption are characterized by the change of the occupancy of a single particle level, together with the usual $\Delta J=0,1$ dipole selection rule. When an atom is ionized down to the L shell, the method of DTA is computationally feasible, and calculations for bromine L-shell spectra in the DTA scheme were presented by Goldberg, Rozsnyai, and Thompson [1]. In the absence of DTA the spectral lines are defined only in terms of line clusters connecting an initial and final configuration in the DCA scheme. Theoretical estimates for the degree of dispersion of line clusters due to the different angular momentum states were given by Moszkowski [2], and more recently in a series of papers by Buache *et al.* [3–6]. The shape of the line clusters is usually expressed in terms of the second and, in some cases, third moments of the transition strengths, and this method is called the method of *unresolved transition arrays* (UTA's). The method of UTA is very useful for obtaining first-order information about a particular transition array. Its shortcoming is that it can give only the envelope of a transition array, and whether or not there are regions of transparencies in between the peaks of the individual lines of the array is beyond the capability of the UTA to discern.

The algorithm developed by Lanczos [7–11] offers a continuous transition from the method of DCA-UTA to DTA, thus exhibiting whether or not the physical line shapes merge the lines of an array into a continuous profile. In the next section we describe the basics of the Lanczos algorithm together with the physical model upon which it rests. In Sec. III we present computational results for a bromine plasma.

II. THEORY

We assume n bound electrons ($n>2$) in the field of an ion and assume that the Hamiltonian (H) is known. We group the n electrons into core and valence electrons, where the core electrons are characterized by their strong binding energies and by the fact that they completely occupy the core states. We start with a "parent" vector $|p\rangle$ of the n-electron system, which is considered an initial state and which is frequently (but not always) the ground state. For the physical processes of interest herein the $|p\rangle$-state vector will be excited by the electric dipole operator (E1). In general the E1 operator induces a series of one-electron excitations from the parent state producing the daughter basis space. The daughter space is differentiated from the parent space from which it was produced not only by the orbits that are reached but also by the difference in parity between the daughter and parent spaces. In all present considerations $|p\rangle$ will be an eigenstate of the system, i.e.,

$$H|p\rangle=E_p|p\rangle\ . \tag{1a}$$

Now we apply the E1 operator to $|p\rangle$ to produce what we call a collective-state vector for which we use the symbol $|\mathrm{CE1};p\rangle$, where

$$|\mathrm{CE1};p\rangle=(\mathrm{E1})|p\rangle\ . \tag{1b}$$

Clearly the model space in which $|\mathrm{Ce1};p\rangle$ is defined is the daughter space, whereas $|p\rangle$ is defined in the parent space. Furthermore $|\mathrm{CE1};p\rangle$ is not, except in the most trivial cases, an eigenvector of H, but it does contain in it the complete E1 strength. The proof of this statement is very straightforward. (Further exposition can be found in Refs. 10 and 11.) The expression for the total strength S_{tot} is given by the following summation over all the eigenstates $\{|d_j\rangle\}$ in the daughter space,

$$S_{\mathrm{tot}}=\sum_J\langle d_j|(\mathrm{E1})|p\rangle^2 \tag{2a}$$

$$=\sum_j\langle d_j|\mathrm{CE1};p\rangle^2 \tag{2b}$$

$$=\langle\mathrm{CE1};p|\mathrm{CE1};p\rangle\ , \tag{2c}$$

where Eq. (2b) uses the definition (1b) and Eq. (2c), which follows from the completeness theorem. Equation (2c) shows that the total (E1) strength is indeed contained in the collective vector, $|\mathrm{Ce1};p\rangle$. We now write down the expansion of the collective vector in terms of the daughter-space eigenvectors,

$$|\mathrm{CE1};p\rangle=\sum_j |d_j\rangle\langle d_j|(\mathrm{E1})|p\rangle \ . \tag{2d}$$

By its very definition we see that the collective vector will contain no contributions from any of the daughter-space eigenvectors that do not carry dipole strength. The distribution of this strength can now be examined by using the Lanczos algorithm, as we describe below. The decomposition of the dipole strength is based on the development of a truncated basis set, call the Lanczos set, which begins with an arbitrary "start" vector designated as $|1\rangle$. In our case $|1\rangle$ is the normalized version of $|\mathrm{CE1};p\rangle$ meaning

$$|1\rangle=|\mathrm{Ce1};p\rangle/\langle \mathrm{CE1};p|\mathrm{CE1};p\rangle^{1/2} \ . \tag{3}$$

We now formulate the second Lanczos basis vector by

$$|2\rangle=(H-H_{11})|1\rangle/K_2 \ , \tag{4a}$$

$$H_{11}=\langle 1|H|1\rangle \ , \tag{4b}$$

$$K_2=[(H^2)_{11}-(H_{11})^2]^{1/2}=H_{12} \ . \tag{4c}$$

It is easy to see that $|1\rangle$ and $|2\rangle$ are orthonormal. We proceed forming

$$|3\rangle=[(H-H_{22})|2\rangle-H_{12}|1\rangle]/K_3 \ , \tag{5a}$$

$$K_3=[(H^2)_{22}-(H_{22})^2-(H_{12})^2]^{1/2}=H_{23} \ , \tag{5b}$$

and in general,

$$|i+1\rangle=[(H-H_{ii})|i\rangle-H_{i-1,i}|i-1\rangle]/K_{i+1} \ , \tag{6a}$$

$$K_{i+1}=[(H^2)_{ii}-(H_{ii})^2-(H_{i-1,i})^2]^{1/2}=H_{i,i+1} \ . \tag{6b}$$

In general, if the first vector $|1\rangle$ is an eigenstate of any operator which commutes with the Hamiltonian H (like J), then all the other vectors will be eigenstates of that operator, but of course, not eigenstates of H. However, as shown in the Appendix, the nth Hamiltonian moment of the collective vector $|\mathrm{CE1};p\rangle$ satisfies the equation, for $n<2i_{\max}-1$,

$$\begin{aligned}\langle \mathrm{CE1};p|H^n|\mathrm{CE1};p\rangle&=\sum_k \lambda_k^n\langle q_k|(\mathrm{E1})|p\rangle^2\\&=\sum_j E_j^n\langle d_j|(\mathrm{E1})|p\rangle^2 \ ,\end{aligned} \tag{7}$$

where the summation is over the first $i_{\max}$ "quasieigenvectors" $|q_k\rangle$ and quasieigenvalues λ_k obtained by the diagonalization of the $i_{\max}$ dimensional tridiagonal Lanczos matrix. It is to be emphasized that to get the same quantity using the true eigenvectors $|d_j\rangle$ [see Eq. (2d)] one would have to sum over the entire (daughter) microscopic eigenspace. Equation (7) states the powerful character of the Lanczos algorithm. Using it makes it unnecessary to find the eigenstates of H to have the *exact* first $2i_{\max}$ moments of what is frequently called the strength function for any particular state vector. It is the physics that dictates the character of this state vector, and in our case it is that state vector which contains the entire E1 strength [see Eqs. (2)]. In practice the Lanczos algorithm is useful for many-particle systems when the number of eigenstates for each J can be very large. Diagonalization of the tridiagonal Hamiltonian given by Eqs. (6a) and (6b) leads to a set of fictitious eigenstates that nevertheless conserve the moments given by Eq. (7). It should be noted that the generation of the Lanczos vectors given by Eq. (6b) terminates at N, where N is the dimensionality of the space spanned by the state vectors. In that case the diagonalization of the N dimensional tridiagonal matrix leads to the *exact* eigenstates of the Hamiltonian. Thus the Lanczos algorithm has the attractive feature that the exact eigenstates can be approximated to any degree in terms of moment conservation given by Eq. (7). For the computation of spectral lines this algorithm is applied for the initial and final states of the many-electron system, where the initial and final states are distinguished by promoting an electron from a one-particle level into another in such a way that the parity changes. As stated before, for the initial or parent states we carry the Lanczos algorithm to its full limit, thus the parent states are eigenstates of H.

To summarize the above, the Lanczos algorithm in the upper limit of iterations is equivalent with the method of DTA, in that its lower degree of iterations becomes equivalent with the method of UTA when supplied with the width

$$\begin{aligned}D_{i,f}=[&\langle i|H^2|i\rangle-\langle i|H|i\rangle^2\\&+\langle f|H^2|f\rangle-\langle fH|f\rangle^2]^{1/2} \ ,\end{aligned} \tag{8}$$

where $|i\rangle$ and $|f\rangle$ stand for the quasieigenvectors in the initial and final state, respectively. The beneficial feature of Eq. (8) is that it is the proper UTA width corresponding to the quasieigenvectors $|f\rangle$. If the eigenvectors are true eigenstates of the Hamiltonian H, then the widths are zero.

Next, we concentrate on the Hamiltonian. Our algorithm rests upon the utilization of the average-atom (AA) wave functions to generate the Lanczos state vectors and the matrix elements of our model Hamiltonian. The AA model, which is the starting point of our computational procedure, is described by Rozsnyai [12], and also briefly in Ref. 1. Here it suffices to state that the AA model assumes that the electronic levels are populated according to the Fermi statistics and that the AA problem can be stated by a set of self-consistent equations which are reminiscent of that of an isolated atom in the ground state. Having obtained the self-consistent solution of the AA problem we proceed by separating the electronic levels into core and valence states. Core states correspond to closed shells, and valence states to partially occupied or empty shells. We write the Hamiltonian in the second quantization formalism as

$$H=\sum_{k,l} a_k^\dagger a_l \langle k|T|l\rangle + \tfrac{1}{2}\sum_{k,l,m,n} a_k^\dagger a_l^\dagger a_m a_n \left\langle k,l\left|\frac{1}{|\mathbf{r}_1-\mathbf{r}_2|}\right|n,m\right\rangle , \quad (9)$$

where the summation indices cover only the valence states. In Eq. (9), T stands for the one-particle operator given by

$$T=-\frac{h^2}{2m}\nabla^2-\frac{Z}{r}+V_c(r)+\frac{h^2}{4m^2c^2}\frac{1}{r}\frac{dV_{AA}(r)}{dr}(\boldsymbol{l}\cdot\mathbf{s}) , \quad (10)$$

where Z is the charge of the nucleus and $V_c(r)$ is the potential due to the core electrons, and is given by

$$V_c(r)=\int \rho_c(r')\frac{e^2}{|\mathbf{r}-\mathbf{r}'|}d^3r'+V_{\rm xc}(\rho_c(r)) , \quad (11)$$

where $\rho_c(r)$ is the density of the core electrons. The last term in Eq. (11) stands for the exchange-correlation part, approximated by a local potential which is a unique functional of the electron density. In our model for $V_{\rm xc}$ we adopt the formula of Hedin and Lundqvist [13]. Since we use a representation in which the Lanczos vectors are eigenstates of the $\mathbf{J}^2$ and J_z operators, it is useful to give the matrix elements of the Coulomb interaction in Eq. (9) in a representation where the two-electron wave functions are eigenstates of the same operators. Thus we use

$$\langle\{JM;n_1l_1j_1n_2l_2j_2\}|\frac{1}{|\mathbf{r}_1-\mathbf{r}_2|}|\{n_3l_3j_3n_4l_4j_4;JM\}\rangle = \sum_{k=0}^{\infty}[f_kR^k(n_1l_1j_1;n_2l_2j_2;n_3l_3j_3;n_4l_4j_4)-g_kR^k(n_1l_1j_1;n_2l_2j_2;n_4l_4j_4;n_3l_3j_3)] , \quad (12)$$

where the R^k Slater integrals are given in terms of the radial wave functions $R_{nlj}(r)$ by

$$R^k(n_1l_1j_1;n_2l_2j_2;n_3l_3j_3;n_4l_4j_4)=\int_0^\infty\int_0^\infty \frac{r_<^k}{r_>^{k+1}}R_{n_1l_1j_1}(r_1)R_{n_2l_2j_2}(r_2)R_{n_3l_3j_3}(r_1)R_{n_4l_4j_4}(r_2)r_1^2r_2^2dr_1dr_2 \quad (13)$$

and the f_k and g_k quantities are given by

$$f_k=(-1)^{j_2+j_3+J}(\tfrac{1}{2}l_1j_1\|C^k\|\tfrac{1}{2}l_3j_3)(\tfrac{1}{2}l_2j_2\|C^k\|\tfrac{1}{2}l_4j_4)\times\begin{Bmatrix}j_1 & j_2 & J\\ j_4 & j_3 & k\end{Bmatrix} , \quad (14a)$$

$$g_k=(-1)^{j_1+j_2+2j_4}(\tfrac{1}{2}l_1j_1\|C^k\|\tfrac{1}{2}l_4j_4)(\tfrac{1}{2}l_2j_2\|C^k\|\tfrac{1}{2}l_3j_3)\times\begin{Bmatrix}j_1 & j_2 & J\\ j_3 & j_4 & k\end{Bmatrix} . \quad (14b)$$

In Eq. (12) the brace stands for a completely antisymmetrized two-electron wave function which is an eigenfunction of the $\mathbf{J}^2$ and J_z operators. For the case of two equivalent electrons, only the first term appears in Eq. (12).

Using the Hamiltonian as defined by Eqs. (9)–(14) we create concrete physical electronic states in the following manner. First, we truncate the AA occupational numbers to their nearest integer values creating the most probable atom. In contrast to the AA, the most probable atom is not fictitious but a physically permissible specimen. Next we create different electronic configurations from the most probable atom by promoting and demoting electrons in the valence levels. We also create different charge states by increasing or decreasing the number of valence electrons and repeating the same procedure. In this manner we create a set of parent configurations that define the set of ions before photoabsorption. For each parent configuration we apply the Lanczos algorithm to its extreme limit thus creating the set of parent electronic states. We assume that the plasma is in local thermodynamic equilibrium (LTE), thus the probability of the states is given by the Boltzmann distribution

$$P(J,\alpha)=KG(J)\exp\{-[E(J,\alpha)-N_v(\alpha)\mu]/kT\} , \quad (15)$$

where $E(J,\alpha)$ and N_v are the many-electron energy and the number of valence electrons in a configuration α, respectively, μ is the Fermi level for the electrons in the plasma, and kT is the temperature. In Eq. (15), $G(J)$ is the statistical weight $2J+1$, and the constant K is determined by the normalization condition

$$\sum_{J,\alpha}P(J,\alpha)=1 . \quad (16)$$

Using the procedure described above we generate all the parent states with appreciable probability. We generate the daughter states from the parent states by applying Eq. (1b) and by using the E1 operator in its second quantization form

$$(\mathrm{E1})=e\sum_{k,l}a_k^\dagger a_l\langle k|\mathbf{r}|l\rangle , \quad (17)$$

where the summation index k goes over a truncated number of unoccupied valence orbitals and the index l goes over the set of occupied valence orbitals. The above restriction with regard to the indices assures that $(\mathrm{E1})|p\rangle$ will be completely in the truncated daughter space. For

each (E1)$|p\rangle$ we apply the Lanczos algorithm either to its extreme limit, this generating all the daughter eigenstates, or by performing only a few Lanczos iterations, thus generating a lesser number but moment conserving quasieigenstates in the daughter space. A detailed description of the Lanczos algorithm together with the description of the computer code CRUNCHER was reported by Resler and Grimes [14], and the reader is referred to this reference for further details. We calculate the oscillator strengths connecting the parent and daughter states and for the computation of photoabsorption we have to supply the oscillator strengths with reasonable line-shape profiles. Also, in a real plasma the bound-bound cross sections are superimposed on the bound-free, free-free, and scattering cross sections. The computation of spectrum profiles and continuous absorption is described by Rozsnyai [15–18], and the reader is referred to the quoted references. In the next section we illustrate our algorithm by presenting some calculations for a bromine plasma.

III. NUMERICAL CALCULATIONS

We apply the method described in Sec. II to a bromine plasma when partially filled L shells occur. We study two cases: (A) $kT=270$ eV and 2.6×10^{-2} g/cm^3 density, and (B) $kT=500$ eV and 3.12 g/cm^3, which corresponds to the metallic density. Under the plasma conditions corresponding to case A experimental emission data were reported by Bailey *et al.* [19]. Intermediate-coupling calculations for case A were reported in Ref. 1, however, in the present report we account for about twice as many parent configurations as in Ref. 1. In Tables I and II we give

TABLE I. Parent configurations, number of bound electrons, and probabilities for bromine at $kT=270$ eV and 2.6×10^{-2} g/cm^3 N_b stands for the number of bound electrons and the numbers in square brackets are exponents of ten.

Configuration	N_b	Number of J states	$\sum_J P(J,\alpha)$
[Ne]3s3p	12	4	1.906[−4]
[Ne](3p)^2	12	5	1.943[−4]
[Ne]3s	11	1	4.842[−3]
[Ne]3p	11	2	1.214[−2]
[He](2s)^2(2p)^5(3s)^2	11	2	4.921[−5]
[Ne]	10	1	2.570[−1]
[He](2s)^2(2p)^{5}3s	10	4	9.842[−3]
[He]2s(2p)^{6}3s	10	2	1.477[−3]
[F]	9	2	4.024[−1]
[He]2s(2p)^6	9	1	6.126[−2]
[He](2s)^2(2p)^{4}3s	9	8	4.230[−3]
[He]2s(2p)^{5}3s	9	6	6.914[−5]
[O]	8	5	1.492[−1]
[He]2s(2p)^5	8	4	5.986[−2]
[He](2p)^6	8	1	2.244[−3]
[He](2s)^2(2p)^{3}3s	8	10	6.888[−4]
[He](2p)^{5}3s	8	4	5.464[−5]
[N]	7	5	1.676[−2]
[He]2s(2p)^4	7	8	1.385[−2]
[He](2p)^5	7	2	1.368[−3]
[C]	6	5	6.015[−4]
[He]2s(2p)^3	6	10	9.704[−4]
[He](2p)^4	6	5	1.974[−4]
[B]	5	2	2.516[−2]
[He]2s(2p)^2	5	8	9.170[−2]
[He](2p)^3	5	5	4.088[−2]
[He](2s)^{2}3s	5	1	3.058[−5]
[He](2s)^{2}3p	5	2	8.214[−5]
[He](2p)^{2}3s	5	8	2.539[−4]
[Be]	4	1	1.564[−3]
[He]2s2p	4	4	1.476[−2]
[He](2p)^2	4	5	1.330[−2]
[He]2s3p	4	4	4.108[−5]
[He]2p3s	4	4	3.465[−5]
[Li]	3	1	6.307[−4]
[He]2p	3	2	1.471[−3]

TABLE II. Same as Table I at $kT=500$ eV and at 3.12 g/cm^3.

Configuration	N_b	Number of J states	$\sum_J P(J,\alpha)$
[Ne]3s3p	12	4	2.446[−4]
[Ne](3p)^2	12	5	2.723[−4]
[Na]	11	1	1.273[−3]
[Ne]3p	11	2	3.445[−3]
[Ne]	10	1	1.622[−2]
[He](2s)^2(2p)^{5}3s	10	4	9.024[−3]
[He]2s(2p)^{6}3s	10	2	1.950[−3]
[He](2s)^2(2p)^4(3s)^2	10	5	4.561[−4]
[F]	9	2	9.985[−2]
[He]2s(2p)^6	9	1	2.172[−2]
[He](2s)^2(2p)^{4}3s	9	8	1.956[−2]
[He](2p)^{6}3s	9	1	5.717[−4]
[He](2s)^2(2p)^3(3s)^2	9	5	4.454[−4]
[O]	8	5	1.979[−1]
[He]2s(2p)^5	8	4	1.032[−1]
[He](2p)^6	8	1	5.570[−3]
[He](2s)^2(2p)^{3}3s	8	10	1.659[−2]
[He](2p)^{5}3s	8	5	2.414[−3]
[N]	7	5	1.384[−1]
[He]2s(2p)^4	7	8	1.499[−1]
[He](2p)^5	7	2	2.043[−2]
[He](2s)^2(2p)^{2}3s	7	8	5.805[−3]
[He](2p)^{4}3s	7	8	3.118[−3]
[C]	6	5	4.206[−2]
[He]2s(2p)^3	6	10	8.523[−2]
[He](2p)^4	6	5	2.291[−2]
[He](2s)^{2}2p3s	6	4	7.951[−4]
[He](2p)^{3}3s	6	10	1.575[−3]
[B]	5	2	5.002[−3]
[He]2s(2p)^2	5	8	2.000[−2]
[He](2p)^3	5	5	1.005[−2]
[He](2p)^{2}3s	5	8	3.285[−4]
[He]2s2p	4	4	1.836[−3]
[He](2p)^2	4	5	1.820[−3]

the electronic configurations and probabilities of all the parent configurations that were considered for the explicit treatment of the Lanczos algorithm. Daughter configurations were generated from each parent configuration by considering all the possible $n \rightarrow n'$ transitions where the principle quantum numbers n and n' are 2, 3, and 4. We assume that under the plasma conditions we are considering the above lines are the strongest. The rest of the spectral lines we treated as one-electron transitions between AA states. It is important to keep in mind that the electronic configurations given in Tables I and II are not those of isolated ions, but ions in the plasma with the free electrons around them perturbing the isolated ion states. In addition to the free electrons, we also keep the AA populations of the sparsely populated upper Rydberg states, which produces additional perturbation on the electronic states of the valence configurations. In order to obtain meaningful photoabsorption cross sections the free-free (inverse bremsstrahlung), bound-free (photoionization), and Compton scattering cross sections were also calculated. The free-free and scattering processes were calculated in the AA approximation, whereas the bound-free processes were calculated explicitly for each parent configuration.

Figures 1–3 summarize the calculated photoabsorption for case A. In Fig. 1, we show when the Lanczos iterations were carried out to the maximum both for the parent and daughter configurations. This corresponds to a full DTA calculation, and using the parent configurations given in Table I, the number $2 \rightarrow 3$ and $2 \rightarrow 4$ transitions was 12 999. Figures 2 and 3 show the results for the daughter configurations when the Lanczos algorithm was stopped after 5 iterations yielding only 1661 $2 \rightarrow 3$ and $2 \rightarrow 4$ transitions. The only difference between Figs. 2 and 3 is the absence or presence of the UTA widths in the individual line shapes, as given by Eq. (8), respectively, and, as shown, the difference is consider-

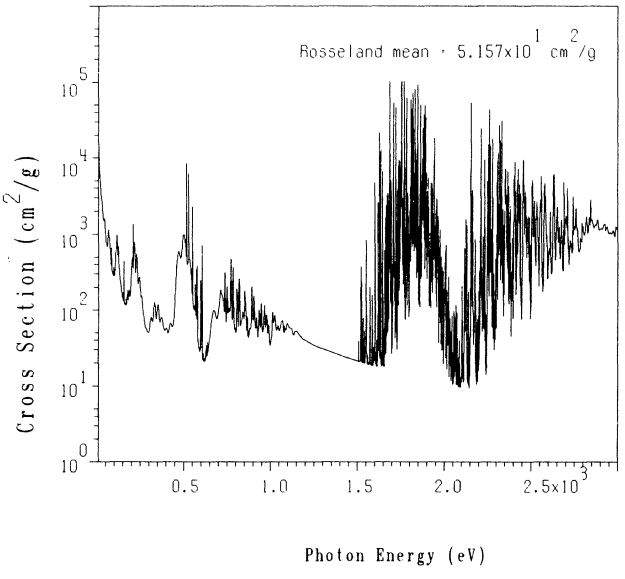

FIG. 1. Computed photoabsorption cross section of bromine at 2.6×10^{-2} g/cm^3 density and at $kT = 270$ eV. the $2 \rightarrow 3$ and $2 \rightarrow 4$ transitions were computed in a full DTA treatment, yielding 12 999 lines. The other lines were calculated in the AA approximation.

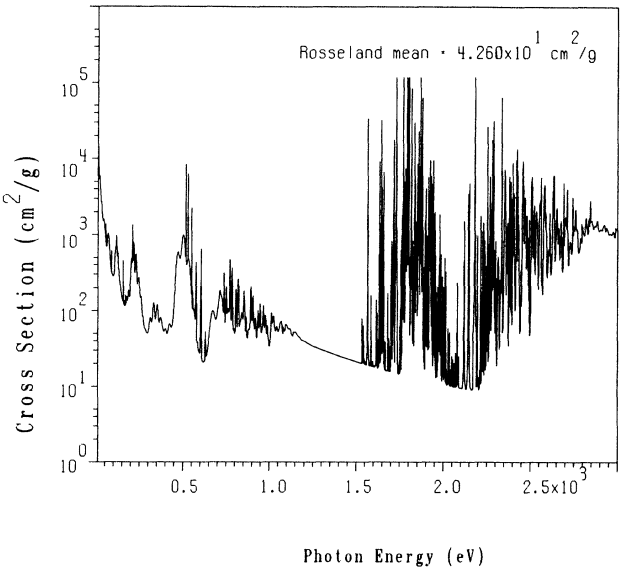

FIG. 2. Same as Fig. 1 with only five Lanczos iterations for the daughter states, yielding 1661 $2 \rightarrow 3$ and $2 \rightarrow 4$ lines. The lines have only the physical (Doppler, Stark, and electron impact) broadening without the UTA widths.

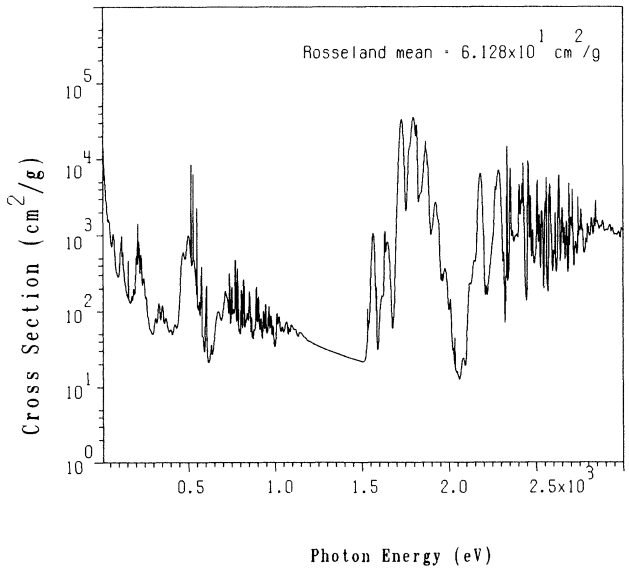

FIG. 3. Same as Fig. 2 with the UTA broadening given by Eq. (8) included in the individual line widths.

able. Above each photoabsorption plot we also give the Rosseland mean opacity, which is important for radiation-transport calculations. At this point we digress briefly and make a few remarks about the line-shape functions.

We assume that the Doppler and UTA broadenings, when applied, yield Gaussian line shapes with the squares of the widths adding up to an effective Gaussian width. In addition, we convolute the Gaussian shapes with the Lorentzian shapes due to the electron impact and by the Stark profiles due to the positively charged ions. The computation of the Doppler width is trivial, and we use the UTA widths as given by Eq. (8), which is part of the Lanczos algorithm. The electron impact and Stark profiles are calculated for the AA levels as described in Ref. [16], and we use the same Stark and electron-impact profiles for each $nl \rightarrow n'l'$ transition. Consequently, our line profiles are not exact for a specified $J \rightarrow J'$ transition; however, we feel that they are adequate for the analysis presented in this paper.

To compare our calculations with experimental measurements, we calculated the emission spectrum from the plasma by using a simple solution of the radiative-transfer equation given by

$$I(\nu)=B(\nu)\{1-\exp[-\sigma(\nu)\rho L]\} , \tag{18}$$

where $I(\nu)$ is the intensity of the emerging radiation, $B(\nu)$ is the Planck function, $\sigma(\nu)$ the frequency-dependent photoabsorption cross section, ρ is the matter density, and L is the average distance inside of the plasma through which the photons must pass before emerging and reaching the detector. Figure 4 summarizes our calculations for the emission. Figure 4(a) shows the experimentally measured emission spectrum published in Ref. [19]. The analysis of lines is also given in Ref. [19]—here it is sufficient to state that the lines are from neonlike to carbonlike configurations and that the free electron density was estimated to be about 5×10^{21} cm^{-3}. Our LTE model at $kT=270$ eV and at 2.6×10^{-2} g/cm^{-3} density mimics the experimental conditions fairly well. Figures 4(b)–4(d) show the calculated emission as predicted by Eq. (18) with $\sigma(\nu)$ corresponding to Figs.

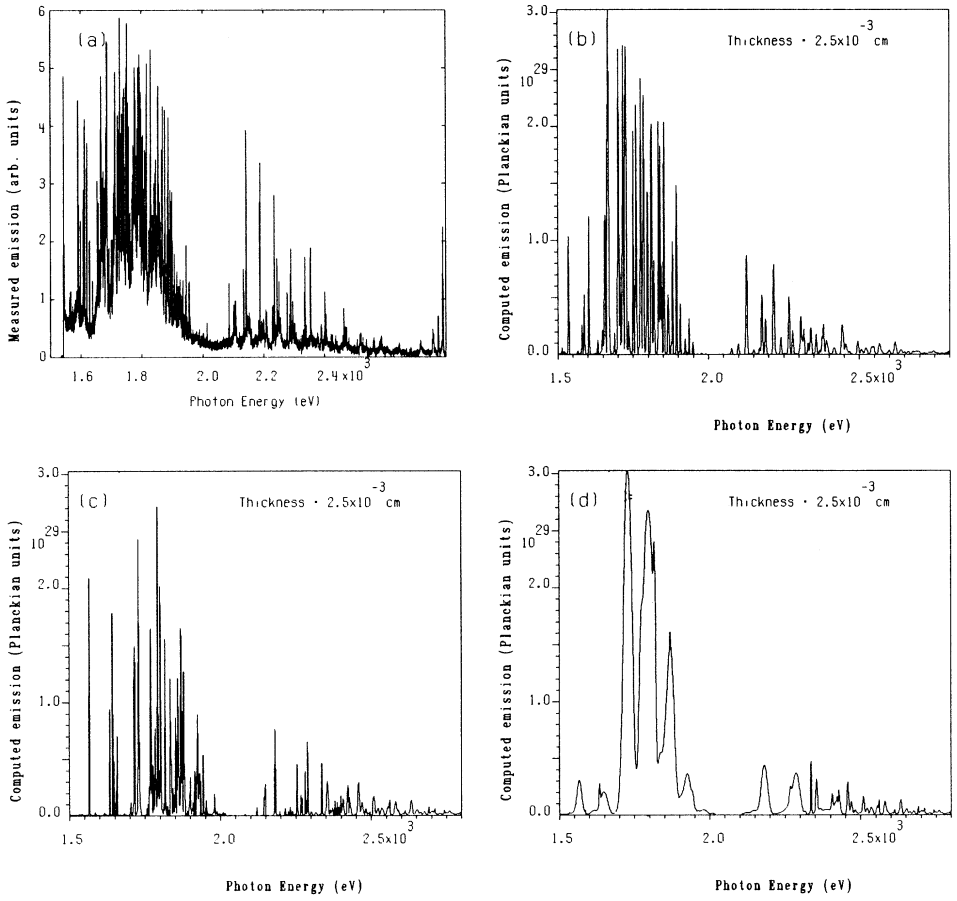

FIG. 4. Measured, computed, and emitted from a bromine plasma. The experimental measurement of frame (a) was reported in Ref. [19], the predicted emission spectra of frames (b), (c), and (d) were calculated by using Eq. (18) and the theoretical cross sections of Figs. 1, 2, and 3, respectively. For L, the value 2.5×10^{-3} cm was taken corresponding to the experimental conditions.

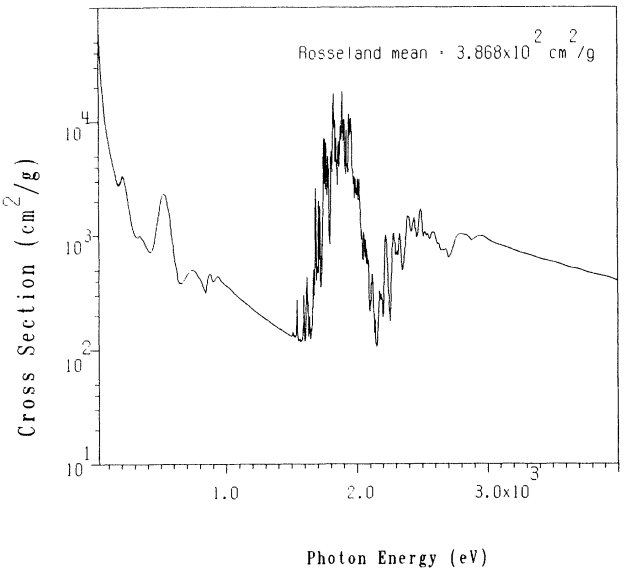

FIG. 5. Same as Fig. 1 at 3.12 g/cm^3 density and at $kT=500$ eV. Again, as in Fig. 1 the $2\rightarrow3$ and $2\rightarrow4$ transitions were computed in the full DTA limit yielding 20 666 lines.

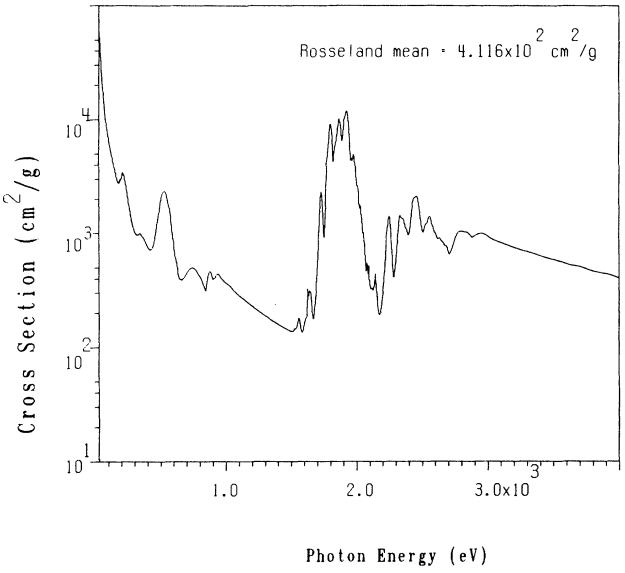

FIG. 7. Same as Fig. 6 with the UTA widths included in the individual line widths.

1, 2, and 3, respectively. For L we took 2.5×10^{-3} cm corresponding to the experimental conditions.

Figures 1–3 illustrate the differences in the predictions of a precise DTA, corresponding to Fig. 1, and between representing the spectral arrays with a smaller number of lines without or with UTA broadening. Although visually there is not much difference between Figs. 1 and 2, the difference in the predicted Rosseland mean opacities is more than 20%. The effect of broadening the lines with the UTA widths is obvious in Fig. 3. With regard to spectroscopic agreement between theory and experiment, it seems that in the low-density plasmas corresponding to our case study A, the application of the UTA widths predicts too smooth spectral features compared with the experiment, as is evident in Fig. 4.

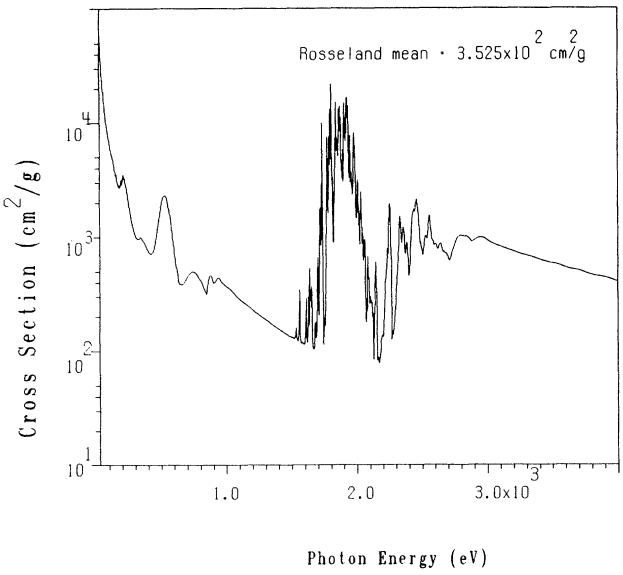

FIG. 6. Same as Fig. 5, but with only five Lanczos iterations for the daughter space yielding 2801 $2\rightarrow3$ and $2\rightarrow4$ lines, and without the inclusion of the UTA widths.

The purpose of our case study B was to investigate whether or not in a high-density plasma the increased physical line widths render the UTA method more applicable. We increased the bromine density to that of metallic bromine and at the same time we increased the temperature to 500 eV so that the Boltzmann distribution of the absorbing specimen is more or less the same as in case A. Figures 5–7 summarize the calculations for this second case study. Figure 5 shows the photoabsorption cross section at metallic density, 3.12 g/cm^3 and at $kT=500$ eV in the full DTA limit of the Lanczos algorithm. The number of computed $2\rightarrow3$ and $2\rightarrow4$ spectral lines was 20 666. Figures 6 and 7 show the calculations for the same condition but with only five Lanczos iterations for the daughter states. In that case, the number of predicted $2\rightarrow3$ and $2\rightarrow4$ lines was only 2801. Again, the difference between Figs. 6 and 7 is the absence or presence of the UTA widths as given by Eq. (8). There is very little visible difference between Figs. 5 and 6 despite the large difference in the number of $J\rightarrow J'$ lines, which were treated explicitly. This is due to the fact that the strong lines show up after a few Lanczos iterations, and the increased pressure broadening has the tendency to smear out the effect of the weak lines. The inclusion of the UTA widths still has a visible smoothing effect, as is evident from Fig. 7, but the effect is not as dramatic as is the low-density case. It should be noted that for case study B

the cross section of Fig. 5 should be regarded as the most precise, and the inclusion of the UTA widths for the lesser number of quasilines, as given in Fig. 7 appears to smear out some structures in the photoabsorption curve.

IV. DISCUSSION

We have demonstrated that the Lanczos algorithm provides a flexible and continuous way to study spectral arrays in between the DCA and DTA limits. This flexibility in accounting in the case of a large number of lines in a spectral array is the most powerful and attractive feature of the Lanczos algorithm. It is generally believed that in the absence of a full DTA treatment the spectral arrays have to be broadened by the proper UTA widths. In the two examples shown in this report we have shown that the inclusion of the UTA widths has the tendency to smear out too much structure, which in turn affects the spectroscopic fidelity and Rosseland mean opacity as well. Naturally, the accuracy of the analysis rests upon the accuracy of the physical line shapes, which we believe to be reliable in our calculations.

ACKNOWLEDGMENTS

This work was performed under the auspices of the U.S. Department of Energy by the Lawrence Livermore National Laboratory under Contract No. W-7405-ENG-48.

APPENDIX: THE MOMENT CONSERVATION THEOREM

In the following we demonstrate that the Lanczos approximation to the full Hamiltonian exactly conserves the Hamiltonian moments of the full eigenspace up to the $2N$th moment, where N is the number of iterations pursued in the application of the Lanczos algorithm (see Sec. II). We use the symbol $M_n(X)$ for the nth Hamiltonian moment for a given state vector $|X\rangle$, not necessarily an eigenvector,

$$M_n = \langle X|H^n|X\rangle \ . \tag{A1}$$

It then follows that M_n is given by the following n-multiple sum over all the N_e eigenvectors $\{|e_j\rangle\}$ of H, where N_e is the dimensionality of the eigenspace,

$$M_n = \sum_{i,j,\ldots,k} \langle X|H|e_i\rangle\langle e_i|H|e_j\rangle \cdots \langle e_k|H|X\rangle \ , \tag{A2}$$

where the summation goes over the internal indices $i,j,\ldots,k$. Now let us identify $|X\rangle$ as $|l_1\rangle$, the first Lanczos vector, which is, after all, a matter of choice. Further, let us assume we pursue the Lanczos algorithm to the largest number of iterations possible, which is, of course, N_e. In that case the set of Lanczos basis vectors $\{|l_k\rangle\}$ constitutes a complete basis for the same space spanned by the eigenbasis $\{|e_j\rangle\}$. Therefore we can reexpress M_n in an expansion in the Lanczos basis as follows:

$$M_n = \sum_{i,j,\ldots,k} \langle l_1|H|l_i\rangle\langle l_i|H|l_j\rangle \cdots \langle l_k|H|l_1\rangle \ . \tag{A3}$$

Now because of the tridiagonality of H in the Lanczos basis the sequence in Eq. (A3) $\{|l_1\rangle, |l_2\rangle, \ldots, |l_N\rangle\}$ is *complete* for $n < 2N-1$ so that the multiple sum of Eq. (A2) terminates at the $(2n-1)$th index. [For example, there are only four terms contributing to Eq. (A2) for $n=3$ and the highest value of l_j is 2.] Thus an expansion to the Nth iteration via the Lanczos algorithm is equivalent to an expansion of the so-called strength function of a particular state vector up to the $2N$th Hamiltonian moment, if we include the zero-order moment $\langle X|X\rangle$ as the first. This first moment was identified with the total strength in Sec. II.

As we have seen it is not necessary to diagonalize the Lanczos Hamiltonian to get the Lanczos quasieigenvectors (as we call them) $|q_j\rangle$ and their associated quasieigenvalues λ_j, in order to evaluate the moment M^n. However, if this is done the expression for M_n simplifies since all off-diagonal contributions to Eq. (A2) in the quasieigenvector representation disappear. This explains the simpler form of Eq. (7) in the text.

[1] A. Goldberg, B. F. Rozsnyai, and P. Thompson, Phys. Rev. A **34**, 421 (1986).
[2] S. A. Moszkowski, Prog. Theor. Phys. **28**, 1 (1962).
[3] C. Bauche-Arnoult, J. Bauche, and M. Klapisch, Phys. Rev. A **10**, 242 (1979).
[4] C. Bauche-Arnoult, J. Bauche, and M. Klapisch, Phys. Rev. A **25**, 264 (1982).
[5] J. Bauche, C. Bauche-Arnoult, E. Luc-Koenig, J. F. Wyart, and M. Klapisch, Phys. Rev. A **28**, 829 (1983).
[6] J. Bauche and C. Bauche-Arnoult, J. Phys. B **20**, 1659 (1987).
[7] C. Lanczos, J. Res. Natl. Bur. Stand. **45**, 255 (1950).
[8] S. D. Bloom and A. Goldberg, Phys. Rev. A **34**, 2865 (1986).
[9] S. D. Bloom and A. Goldberg, Phys. Rev. A **36**, 3152 (1987).
[10] S. D. Bloom and R. F. Hausman, Jr., in *Moment Methods in Many-Fermion Systems,* edited by B. J. Dalton *et al.* (Plenum, New York, 1979), p. 151.
[11] R. R. Whitehead, in *Moment Methods in Many-Fermion Systems* (Ref. [10]), p. 235.
[12] B. F. Rozsnyai, Phys. Rev. **145**, 1137 (1972).
[13] L. Hedin and B. I. Lundqvist, J. Phys. C **4**, 2064 (1971).
[14] D. A. Resler and S. M. Grimes, Comput. Phys. **2**, 65 (1988).
[15] B. F. Rozsnyai, J. Quant. Spectrosc. Radiat. Transfer **13**,

1285 (1973).
[16] B. F. Rozsnyai, J. Quant. Spectrosc. Radiat. Transfer **17**, 77 (1977).
[17] B. F. Rozsnyai, J. Quant. Spectrosc. Radiat. Transfer **19**, 641 (1978).
[18] B. F. Rozsnyai, J. Quant. Spectrosc. Radiat. Transfer **22**, 337 (1979).
[19] J. Bailey, R. E. Stewart, J. D. Kilkenney, R. S. Walling, T. Phillips, R. J. Fortner, and R. W. Lee, J. Phys. B **19**, 2639 (1986).